PAPER

Check for updates

Sludge-derived hydrochar as a potential electrocatalyst for improved CO_2 reduction in microbial electrosynthesis†

Lakshmi Pathi Thulluru,[a] Anil Dhanda,[b] Manikanta M. Doki,[b] Makarand M. Ghangrekar [iD] [abc] and Shamik Chowdhury [iD] *[a]

Microbial electrosynthesis (MES) is a progressive technology that can sequester carbon dioxide (CO_2) to produce high-value multi-carbon organic compounds. However, the limited organic production rate is the primary bottleneck, limiting the real-life application of this technology. To overcome this challenge, the present investigation explores sludge-derived hydrochar as a cathode catalyst to enhance CO_2 bioreduction in MES. The hydrochar composite synthesized using anaerobic sludge (ANS) and alum sludge (ALS) exhibited excellent electrochemical properties with higher limiting current density and lower charge transfer resistance. Additionally, key structural properties, such as elevated specific surface area, abundant surface functional groups, and the presence of nitrogen in the form of pyridinic and graphitic nitrogen, are primarily responsible for enhancing the organic product synthesis in MES. Furthermore, the hydrochar composite catalyzed MES resulted in an acetate production of 41.14 ± 5.03 mM L^{-1}, which was nearly twice that of the uncatalyzed MES. Moreover, the current and carbon recovery efficiencies were found to be 52.44% and 45.44%, which were 1.47 and 2.44 times that of uncatalyzed MES. These results demonstrate the potential of sludge-derived hydrochar as a promising cathode electrocatalyst for enhancing CO_2 bioreduction in MES.

Sustainability spotlight

Technologies for carbon capture, utilization, and sequestration are essential for achieving Sustainable Development Goal (SDG) #13, as they help mitigate climate change by reducing carbon dioxide (CO_2) emissions. Within this framework, microbial electrosynthesis (MES) stands out as a promising advanced bioelectrochemical technology that transforms CO_2 into valuable chemicals using renewable energy. MES achieves CO_2 bioreduction with the aid of homo-acetogens, generating multi-carbon compounds and byproducts like H_2. This study explores the use of hydrochar derived from anaerobic and alum sludge as a cost-effective and sustainable electrocatalyst for MES. The method of producing hydrochar from waste sludge, sourced from water and wastewater treatment facilities, supports SDG #9 by tackling challenges related to industry, innovation, and infrastructure, and demonstrates its potential for scalability in practical MES applications.

1. Introduction

Carbon capture, utilization, and sequestration (CCUS) technologies are crucial to reduce anthropogenic carbon dioxide (CO_2) emissions and combat climate change.[1] In this context, bioelectrochemical systems (BES) represent a potential CCUS option to attenuate the carbon footprint of wastewater treatment plants (WWTPs).[2] Particularly, microbial electrosynthesis (MES), a bifurcation of BES, has attracted immense scientific interest because of its ability to convert CO_2 to value-added chemicals by using electricity derived from renewable resources. A typical MES comprises a two-chambered system that allows the migration of protons and electrons emerging from the anode during a non-spontaneous water-splitting reaction towards the negatively charged cathode via a proton exchange membrane and external circuit, respectively. Introducing homoacetogens in the cathodic chamber reduces CO_2 by utilizing the electrons and protons approaching from the anodic end and produces multi-carbon compounds, including carboxylic acids and byproducts like hydrogen (H_2). Additionally, other products, such as alcohol and polyhydroxy alkanoates, are also synthesized.[3] Thus, the MES presents a one-point solution for wastewater treatment, CCUS, and producing valuable chemicals.

[a]School of Environmental Science and Engineering, Indian Institute of Technology Kharagpur, Kharagpur, West Bengal 721302, India. E-mail: shamikc@iitkgp.ac.in

[b]Department of Civil Engineering, Indian Institute of Technology Kharagpur, Kharagpur, West Bengal 721302, India

[c]National Institute of Technology Puducherry, Karaikal, Puducherry 609609, India

Despite the enormous potential, the technology is still in its infancy due to low product synthesis rates owing to (i) insufficient microbial loading, (ii) sluggish electrochemical reaction kinetics, and (iii) low mass transfer efficiencies of CO_2 and H_2.[4,5] Consequentially, intensive attempts have been made to address these roadblocks by using different strategies, including the application of cathodic electrocatalysts, varying the applied cathodic potential, and tuning reactor design. Introducing cathode electrocatalysts demonstrating exemplary traits of high specific surface area (SSA) and excellent conductivity embodying catalytically active sites can enhance the product synthesis rate by lowering the electron transfer resistance from the electrode to the biofilm.[6] Other strategies like regulating the cathodic potential to tune the H_2-mediated electron transfer mechanism, modifying reactor design by reducing electrode distances, and increasing the CO_2 contact time with the solid electrode can also improve CO_2 reduction in MES.[7]

The efficacy of CO_2 reduction directly hinges on the ease of electron transfer between the cathode and biofilm. Besides, the electron transfer pathways of homoacetogens are also swayed by the traits of the cathode material. The attributes of electrocatalyst ink coated on the conventional carbon-based cathode surface must possess some distinct characteristics, including high SSA, good biocompatibility, exceptional chemical and mechanical stability, affordability, and remarkable electrical conductivity to ease the electron transfer mechanism.[8,9] The prominently used electrocatalysts that have exhibited these exceptional traits include chitosan, reticulated vitreous carbon, carbon nanotubes, reduced graphene oxide–tetraethylene pentamine, metal oxides, and nickel foam.[10–17] However, extensive application of these surface-modified materials is often limited by their complex and energy-intense synthesis, resulting in higher costs and unsuitability for field-scale applications.[18] Additionally, although electrocatalysts derived from waste-derived materials like biochar, sewage, and alum sludge (ALS) have proved their efficacy in other BES, such as microbial fuel cells (MFCs), there is limited research on their applicability in MES.[19,20] Hydrochar, for instance, has a rich surface chemistry compared to biochar due to the use of relatively lower temperatures (180–250 °C) during hydrothermal carbonization (HTC).[21,22] This thermochemical conversion of biomass predominantly involves reactions such as decarboxylation, dehydration, decarbonylation, demethoxylation, intermolecular rearrangement, condensation, and aromatization, among others.[23] Notably, hydrochar derived from anaerobic sludge (ANS) can augment the presence of acetogenic bacteria and improve the buffering capacity in anaerobic digestion.[23] Additionally, the high SSA and porosity of hydrochar can facilitate the interaction of microorganisms by immobilizing them on the surface.[21] Furthermore, CO_2 adsorption over the surface depends on physicochemical properties, such as SSA, pore size, presence of functional groups, and aromaticity.[24] On the other hand, ALS has emerged as an economical adsorbent for treating various contaminated water- and soil-borne inorganics, such as perchlorate, selenium, arsenic, phosphorus, fluoride, and heavy metals.[25] Further, it also successfully demonstrated potential as an effective material for CO_2 adsorption.[26] Given these characteristics, hydrochar synthesized using these precursors holds potential as an electrocatalyst in MES.

However, there are very limited investigations on the application of waste derived catalysts to promote CO_2 bioreduction in MES. For example, Tahir et al. (2021) employed a rice straw-derived biochar monolith coated with MXene as a carbon-based cathode in MES.[27] The MXene-coated biochar resulted in high butyrate production (1173 mg L^{-1}), attributed to the increased SSA of MXene-coated biochar (64 m^2 g^{-1}) and its high electrical conductivity. Additionally, incorporating a wood chip-based functionalized biochar cathode boosted single-cell protein production in MES. This process effectively utilized CO_2 (39 ± 2%) from anaerobic digestion and nitrogen (6.7 ± 0.8%) from livestock effluents.[28] Moreover, using an iron–carbon micro-electrolysis matrix combined with coconut shell biochar facilitated cathodic CO_2 reduction in BES, enabling the in situ use of the synthesized products by heterotrophic denitrifiers for denitrification.[29] However, it is worth noting that using exotic materials, such as MXene, can raise the overall cost of the process. Additionally, producing biochar in these cases is more energy-intensive compared to hydrochar. Therefore, investigating waste-derived carbon-based materials that follow a facile synthesis procedure and demand less energy could be a cost-effective alternative for low-cost hydrochar production.

Based on the aforementioned discussion, the present investigation examines the efficacy of ANS and ALS-derived hydrochar as a cathode electrocatalyst to reduce CO_2 to acetic acid in MES. The catalyst was synthesized in a facile manner using HTC and intensively investigated using different physicochemical and electrochemical characterizations. This advocated the enhanced performance concerning the observed current response and acetate accumulation in MES. The results obtained from this investigation provide an original direction toward exploring waste-derived electrocatalysts for CO_2 reduction in MES.

2. Experimental

2.1. Materials

All chemicals employed in the present investigation were analytically pure and utilized without additional processing. Their detailed information is provided in the ESI.†
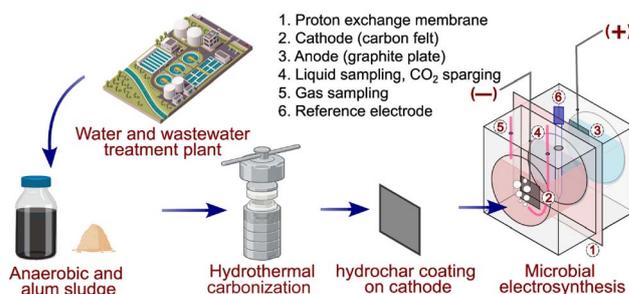

Fig. 1 Schematic of ANLS synthesis by hydrothermal carbonization of ANS and ALS, and coating over a cathode for application in MES.

2.2. Synthesis of hydrochar

The ANS-based hydrochar was first synthesized at 230 °C for 4 h using 30 mL of 36.38 g L^{-1} settled ANS in a 50 mL stainless-steel autoclave, giving a hydrochar yield of 76.96% (Fig. 1). This yield assisted in quantifying the mass of powdered ALS to be chosen for varying ratios of ANS and ALS, *viz.*, 1 : 1, 1 : 2, 2 : 1, 1 : 3, and 3 : 1, which were named 'ANLS-1', 'ANLS-2', 'ANLS-3', 'ANLS-4', and 'ANLS-5', respectively. After HTC, the resulting suspension was centrifuged at 5000 rpm, and the pelleted solids were washed multiple times until a near-neutral pH was attained. The composites were then oven-dried overnight at 100 °C and subsequently ground into fine powder using a mortar and pestle.

2.3. Instrumental characterization

The as-prepared hydrochar electrocatalysts were characterized by a wide range of microscopy, spectroscopy, and surface-analytical techniques, as detailed in the ESI.†

2.4. Electrochemical analysis

The electrochemical properties of the as-prepared hydrochars were explored using cyclic voltammetry (CV), linear sweep voltammetry (LSV), and electrochemical impedance spectroscopy (EIS). These measurements were carried out in a three-electrode system, dipped in 1 M potassium chloride (KCl) solution and connected to an electrochemical workstation (Autolab PGSTAT 204, Metrohm Autolab BV, Netherlands). The working electrode consisted of a 2 × 2 cm^2 carbon felt painted with catalyst ink which was connected to a titanium (Ti)-wire (Ø = 0.81 mm) current collector. The catalyst ink comprised the as-synthesized powdered hydrochar (2 mg cm^{-2}), carbon black (0.5 mg cm^{-2}), and polydimethylsiloxane (PDMS, 6.67 μL mg^{-1}) that were added to 10 mL isopropanol solvent and sonicated for 20 min. Further, the reference and counter electrodes were silver/silver chloride (3 M KCl, +0.21 V *vs.* standard hydrogen electrode, SHE) and 0.8 × 0.8 cm^2 platinum (Pt)-plate, respectively. The CV and LSV analyses were performed to observe the current responses by sweeping the working electrode potential from +1.4 to −1.0 V and 0 to −1.0 V *vs.* SHE, respectively, at a scan rate of 50 mV s^{-1}. Additionally, the Nyquist curve plotted using the EIS data revealed the electrolyte (R_s) and charge transfer resistance (R_{ct}).

2.5. Analysis procedure

The procedure to quantify the volatile fatty acids (VFAs) synthesized and headspace gas generated during the experiment is described in the ESI.†

2.6. Bacterial cultivation

The mixed culture inoculum obtained from the up-flow anaerobic sludge blanket (UASB) reactor was initially pretreated by heating at 85 °C for 1 h to eliminate heat-intolerant methanogens. This was followed by chemical inhibition of methanogens by adding 0.5 mM sodium 2-bromoethanesulfonate.[30] The pretreated inoculum was enriched in modified 879 DSMZ

media (ESI†) in 100 mL sterilized serum bottles with 10% (v/v) inoculation and 50 mL working volume. The carbon substrate provided during enrichment was a H$_2$: CO$_2$ (80 : 20 v/v) gas mixture pressurized to 1 atm overpressure, which facilitated the growth of CO$_2$ fixing homoacetogens. This was later verified by acetate accumulation of 828 ± 187 mg L^{-1} and an increase in optical density monitored at 600 nm (OD$_{600}$), reaching 0.35 to 0.40 over 14 days. The enriched culture was then used to inoculate the cathodic chamber of MES.

2.7. Microbial electrosynthesis reactor setup and operation

The anodic and cathodic chambers of the MES were fabricated using two acrylic sheets of 10 cm × 10 cm × 2.5 cm that were bore holed (Ø = 8 cm and depth = 2 cm) to obtain a cylindrical empty volume of 100.5 cm^3. The two sheets were then joined using screws and nuts. A Nafion 117® separator was sandwiched between the sheets, creating two hollow chambers, with working : total volumes of 80 : 100 (Fig. 1 and S1†). A graphite plate and felt (4 × 4 cm^2), each connected to a Ti-wire (Ø = 1.2 mm) current collector, acted as the anode and cathode, respectively. The cathode of MES-ANLS was coated with 2 mg cm^{-2} ANLS-2 on carbon felt, whereas the control MES (*i.e.*, MES-C) consisted of bare carbon felt. The anodic chamber contained one inlet used for anolyte addition and release of oxygen from the anodic chamber. The cathodic chamber was provided with two inlets for supplying the carbon substrate as CO$_2$ (along with catholyte replacement) and headspace gas measurement connected to a 0.5 L gas bag. Both the anolyte and catholyte consisted of a modified 879 DSMZ medium. Additionally, 10% (v/v) enriched inoculum, vitamin, and trace element solutions were added to the catholyte hermetically, and the anaerobicity was maintained by sparging it with nitrogen gas. Further, the anodic and cathodic chambers contained calomel reference electrodes (+0.24 V *vs.* SHE) to measure the cathodic and anodic potentials. The MES was connected to a direct current (DC) power supply and operated at 3.5 V, with a cathodic potential of −0.80 ± 0.05 V *vs.* SHE. The catholyte was sparged daily with CO$_2$ for 20 min at 5 mL min^{-1}.

2.8. Calculation of product yield

The product synthesis of multi-carbon organic compounds, such as acetic acid, propionic acid, and iso-butyric acid, along with H$_2$ in the catholyte was assessed using coulombic or current efficiency (CE) and carbon recovery efficiency (CRE). The synthesis of these multi-carbon organic compounds at any time t was estimated as per eqn (1).[31]

$$n_{product,t} = \frac{V_{catholyte} \times (C_{product,t} - C_{product,t_o})}{M_{product}} \quad (1)$$

Here, $n_{product,t}$ is the number of millimoles (mM) of acetic acid, propionic acid, or iso-butyric acid produced at time t, $V_{catholyte}$ represents the effective volume of the catholyte (mL), $C_{product,t_o}$ and $C_{product,t}$ are the initial and final concentrations (mg L^{-1}) of the product, respectively, and $M_{product}$ is the molar mass (mg) of the product.

The CE (%) quantifies the effectiveness of capturing the cathodic electrons by the homoacetogenic bacteria for synthesizing these products and was determined using eqn (2).[31]

$$CE = \frac{n_{product,t} \times f_{product} \times F}{\int_{t_o}^{t} I dt} \times 100 \qquad (2)$$

In this context, $f_{product}$ represents the molar conversion factor (*i.e.*, 8 electron equivalent for acetic acid, 10 electron equivalent for propionic acid, 12 electron equivalent for iso-butyric acid, and 2 electron equivalent for H_2), F is the Faraday constant $(9.648 \times 10^7 \text{ C mM}^{-1})$, and I is the current (A) supplied to the cathode.

Additionally, the CRE (%) computes the percentage of pure CO_2 that the homoacetogenic bacteria utilize to synthesize the multi-carbon organic compounds in the catholyte and it is approximated using eqn (3).[31]

$$CRE = \frac{n_{product,t} \times f_{C,product}}{n_{CO_2}} \times 100 \qquad (3)$$

Here, $f_{C,product}$ indicates the number of moles of carbon in one mole of product (*e.g.*, 2 for acetic acid, 3 for propionic acid and 4 for iso-butyric acid), and n_{CO_2} is the number of moles of CO_2 sparged into the catholyte at regular intervals.

3. Results and discussion

3.1. Electrochemical characterization

The electrochemical activity of the synthesized catalysts was tested using CV analysis. As shown in Fig. 2a, the highest limiting current density was observed to be -12.56 A m^{-2} for ANLS-2, followed by -8.25 A m^{-2} for ANLS-4, whereas it was only -7.43 A m^{-2} and -2.86 A m^{-2} for pristine ALS and ANS, respectively. The higher current density clearly indicate the role of the composite material in delivering greater current densities at the same applied potential, which was caused by the higher SSA observed for the composite (see Section 3.2). Also, it was noted that the total area covered by the ANLS-2 CV loop was very high compared to other catalysts, indicating the higher charge transfer capacity of the composite.

The LSV of the synthesized catalysts was assessed to gauge their efficacy in H_2 synthesis under the influence of a negative imposed potential. Planktonic cells in the cathodic chamber of the MES receive electrons from the cathode *via* a H_2-mediated pathway. Consequently, an increased concentration of H_2 generated by the catalyzed cathodes will facilitate the provision of more reducing equivalents to the planktonic cells. These then utilize the electrons as reducing equivalents to convert CO_2 into organic compounds. This exemplifies the pivotal role of H_2 and H_2-producing cathodes in influencing the production rate of organic compounds *via* MES. The negative potential, marking a significant drop in the current response in the LSV of the catalyzed electrodes, is regarded as the requisite imposed potential for triggering the H_2 evolution reaction.

The enhanced current response of ALNS-2 could be attributed to its greater electrochemically active surface area (EASA) available for carrying out the reduction reactions. To verify this, the double-layer capacitance (C_{dl}), which is directly proportional to EASA, was estimated.[32] This was determined through
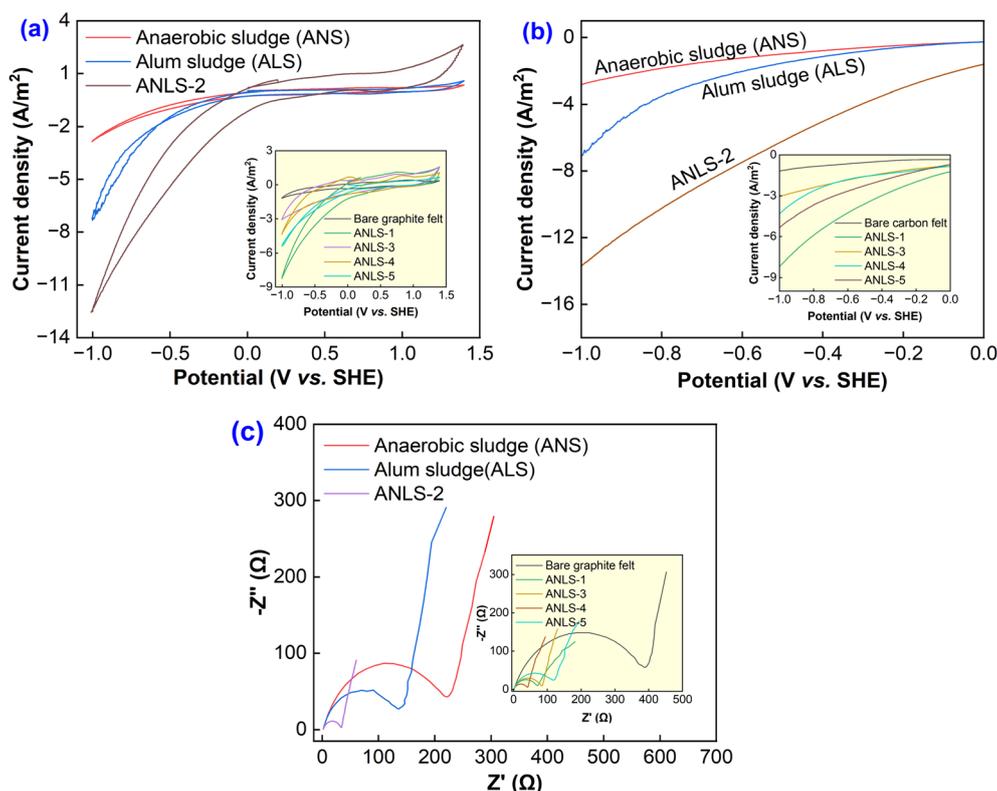

Fig. 2 (a) CV curves, (b) LSV curves, and (c) EIS analysis of the precursors and the as-prepared hydrochar composites.

CV conducted in the non-faradaic range of 0.3 to -0.3 V at different scan rates of 20, 30, 40, 50, 60, 70, 80, and 90 mV s^{-1} (Fig. S2†). The C_{dl} is defined as the slope derived from the linear regression between the differences in current density ($\Delta j/2 = (j_a -j_c)/2$) across different scan rates. Here, j_a and j_c are the limiting current responses at 0.3 V and -0.3 V, respectively. ALNS-2 exhibited a C_{dl} of 1.68×10^{-2} mF (Fig. S2†), which is 11.2 times higher than that of bare carbon felt (1.5×10^{-3} mF), indicating its significantly superior EASA to that of bare carbon felt. Additionally, to evaluate the electrochemical stability of the hydrochar, ANLS-2 was subjected to 100 cycles of CV, showing a 0.26% decrease in current density per cycle (Fig. S3†). This demonstrates the durability and electrochemical stability of the synthesized ANLS-2 hydrochar.

As can be seen in Fig. 2b, there is a slight bend from -0.4 V *vs.* SHE for ANLS-2, indicating the initiation of the H$_2$ evolution reaction at that potential. In contrast, the required applied potential was -1.0 V *vs.* SHE for both pure ANS and ALS

catalysts, indicating that the imposed potential should be at least twice as much for these catalysts for H$_2$ production in MES. Moreover, the ANLS-2 catalyst had the maximum limiting current density of -12.56 A m^{-2} among the synthesized catalysts, which confirmed its superior electrocatalytic activity. This also emphasizes that the catalyst can supply higher current to the microbes, resulting in greater organic compound production.

Further, the EIS analysis assessed the ease of charge migration from the catalyzed electrodes to the biofilm. As shown in Fig. 2c, the Nyquist plot resulted in an R_s of 1.8 Ω for all the catalyzed electrodes, as the electrolyte (1 M KCl) used was identical. Further, the R_{ct} measured from the diameter of the semi-circle for the optimum concentration of ANLS-2 was found to be only 34.0 Ω, which was 6.5 times and 4 times lower than those of the sole ANS and ALS catalyzed electrodes, respectively, and it was also the lowest compared to those of other ratios of ANLS. Thus, based on the electrochemical characterization, a 1 : 2 ratio of ANS
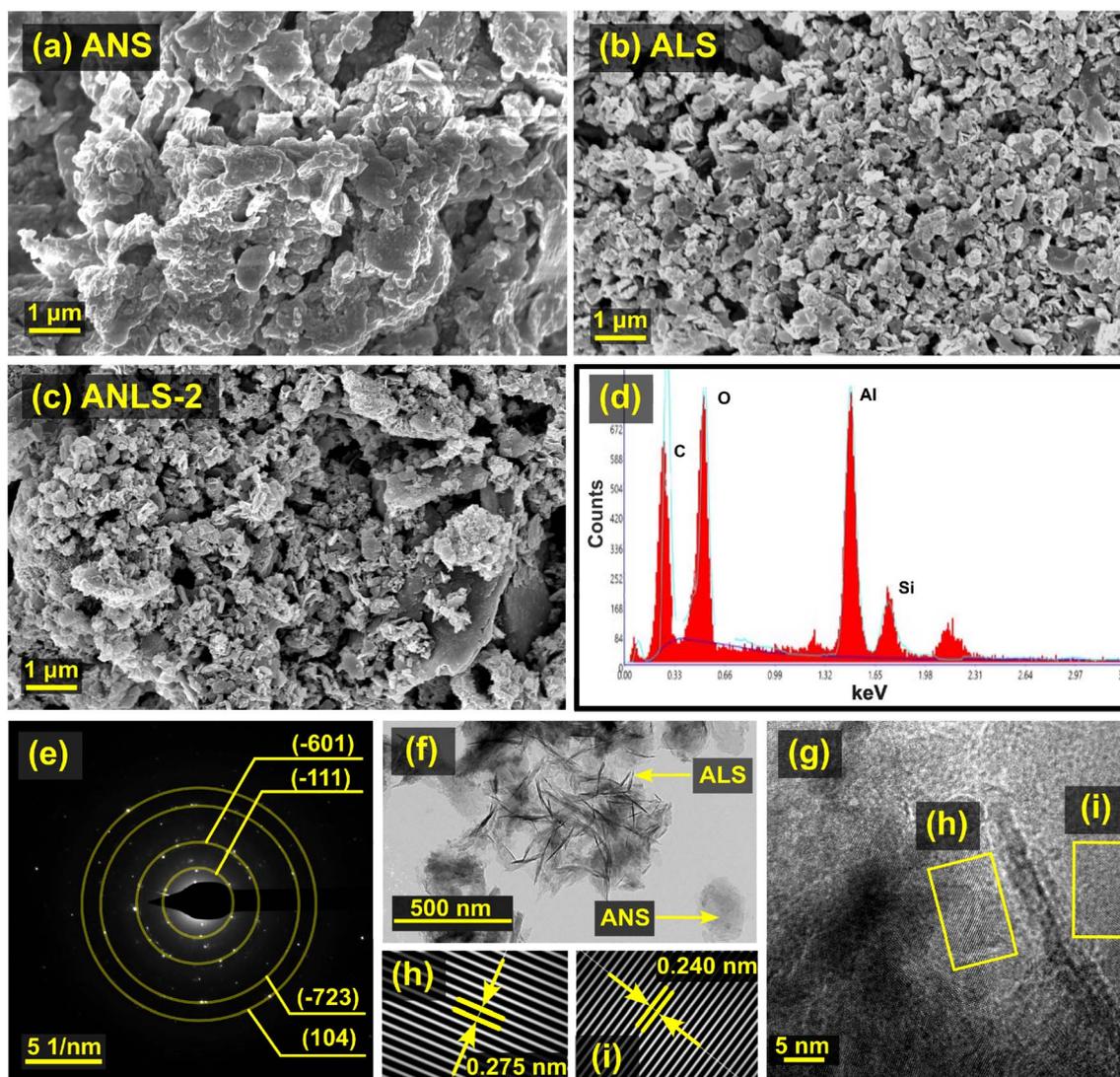

Fig. 3 FESEM images of (a) ANS, (b) ALS, and (c) ANLS-2 hydrochar. (d) EDX spectra of ANLS-2. (e) Selected area electron diffraction pattern and (f) TEM image of ANLS-2. (g) HRTEM image of ANLS-2 hydrochar. (h and i) Fast Fourier Transform (FFT) patterns of ANLS-2 hydrochar.

to ALS in ANLS-2 was found to be optimal for application in MES and, hence, it was utilized for the actual application.

3.2. Characterization of the ANLS hydrochar composite

The FESEM images of the ANS, ALS, and ANLS-2 composites are depicted in Fig. 3. The surface morphology of ANS (Fig. 3a) illustrates smooth, bulk, and loosely agglomerated deposits. In contrast, ALS (Fig. 3b) has a distinct flake-like structure. The characteristic morphology of each precursor is evident in ANLS-2 (Fig. 3c), revealing the successful immobilization of ALS over ANS with an interconnected porous network structure, validating their coexistence in the hydrochar composite. This was also observed in the TEM image of ANLS-2, wherein the presence of thin ALS flakes over the surface of ANS could be seen (Fig. 3f). Further, the Fast Fourier Transform (FFT) patterns obtained from the HRTEM image (Fig. 3g) displayed the stacking of the (−402) planes of calcium silicate, with an interlayer (d) spacing of 0.275 nm (Fig. 3h). Additionally, the interplanar gap of 0.240 nm corresponds to the (110) plane of quartz (Fig. 3i). Moreover, the selected area electron diffraction pattern further validates the existence of calcium silicate (−601), (−723), quartz (104), and muscovite (−111) in the composite ANLS-2 (Fig. 3e). Furthermore, it can be inferred from the EDX analysis (Fig. 3d) that the elemental composition of the ANLS-2 composite is as follows: carbon (C): 22.72%, oxygen (O): 22.85%, aluminum (Al): 45.60%, and silicon (Si): 8.99%.

The X-ray diffraction (XRD) patterns (Fig. 4a) assist in inspecting the amorphous and crystalline structures of the as-prepared sludge-derived hydrochar. In the case of ALS, the sharp peak at 26.51° represents silica and connotes its amorphous structure.[33] However, the XRD profile of ANLS-2 displays several peaks. In particular, quartz in ANS exhibits different phases at 2θ of 20.68° (100), 26.42° (011), 39.31° (102), 50.08° (003), and 68.19° (301) (JCPDS: 043-0596),[34] with d spacings of

0.429, 0.337, 0.229, 0.189, and 0.137 nm, respectively. Similarly, muscovite (mica) displays distinct peaks at 2θ of 19.86° and 26.62° (JCPDS: 07-0025), corresponding to the (020) and (003) planes, respectively.[35] The occurrence of diffraction planes at (013) and (801) at 2θ of 40.59° and 50.23° confirmed the presence of calcium silicate (JCPDS: 043-1460), with d spacings of 0.223 and 0.181 nm, respectively.[36]

Furthermore, the discernible peaks of carbon were present in ANS and ANLS-2 at 2θ of 26.60°, 42.72°, 44.67°, and 77.70° (JCPDS: 02-1076), which can be indexed to (006), (101), (103), and (110) diffraction planes. The corresponding d spacing values are 0.334, 0.211, 0.203, and 0.123 nm, respectively.[37] Meanwhile, silicon sulfide shows a characteristic peak at 2θ of 20.78°, 26.51°, 36.50°, 39.49°, 42.40°, 50.08°, 54.94° and 68.42° (JCPDS: 47-1376), ascribed to (100), (101), (110), (102), (200), (112), (202) and (301), respectively. In addition, carbon azide displays strong diffraction peaks at 26.59°, 54.76°, 60.15° and 73.37° (JCPDS: 01-087-1526), which are representative of (200), (400), (331), and (511) planes. On the other hand, the reflections from the (200), (400), and (511) planes of potassium nitrate appear at 26.59°, 54.76°, and 73.37° (JCPDS: 01-079-1985) for ANS. The diffraction peaks of potassium aluminum silicate are discerned at 2θ of 26.59°, 31.28°, and 49.98° (JCPDS: 01-075-0550), corresponding to (400), (332), and (633) planes, respectively. Thus, the observations from the XRD profile indicate the coexistence of different ANS and ALS phases in the as-prepared composite ANLS-2.

The Fourier transform infrared (FTIR) spectra of ANS, ALS, and ANLS-2 (Fig. 4b) elucidate different surface functional groups.[38] The broad peak between 3700 and 3560 cm^{-1} is associated with the stretching vibration of –OH in the humic substance, especially in ANS, which is eventually presented in ANLS-2.[39] Similarly, a minor but broad absorption band persists between 3600 and 3200 cm^{-1}, associated with the –OH bond due to the adsorbed and structured water in both ALS and
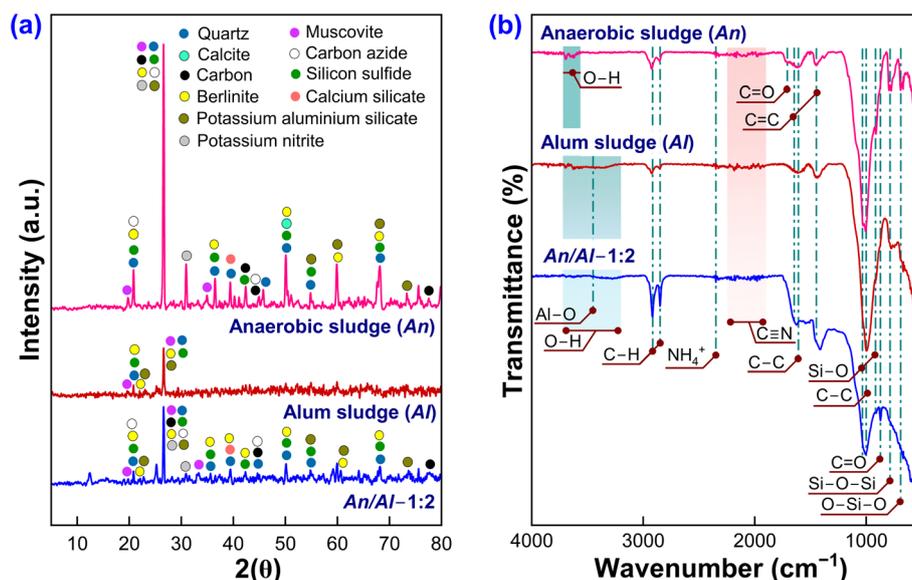

Fig. 4 (a) XRD patterns and (b) FTIR spectra of ANS, ALS, and ANLS-2 hydrochar.

ANLS-2.[40] Along with the broad –OH bond, the Al–O bond is present in both ALS and ANLS-2 at 3440 cm^{-1}. The asymmetrical and symmetrical stretching of C–H bonds in the methyl group appears at 2920 and 2852 cm^{-1}, respectively,[41] while the N$^+$–H stretching vibrations of –C≡N$^+$–H exhibit a mild absorption band at 2362 cm^{-1}.[42] A minor band appearing between 2260 and 1900 cm^{-1} describes the persistence of terminal free cyanide group (–C≡N) in ANS, ALS, and ANLS-2.[43] Further, multiple weak absorbance peaks of C=O are present around 1705 and 873 cm^{-1}, C=C at 1644 and 1445 cm^{-1}, and C–C around 1605 and 1003 cm^{-1} in all of the three hydrochars.[44] These findings exhibit a high degree of aromatization of the as-synthesized hydrochars along with the abundance of oxygen-containing functional groups.[22] Additionally, three silicon-based absorbance peaks, *viz.*, Si–O (1030 and 914 cm^{-1}), Si–O–Si (780 cm^{-1}), and O–Si–O (690 cm^{-1}), are observed.

Electrochemical reactions are surface-sensitive and modify traits like current density per electrode size (or catalytic loading mass), altering the intermediate adsorptions and reaction pathways.[45] Hence, it is quintessential to quantify the SSA as well as the pore size distribution of the as-synthesized hydrochars. The ANS and ANLS-2 hydrochars (Fig. 5a) traced the Type II isotherm based on the classification by the International Union of Pure and Applied Chemistry.[46] The Brunauer–Emmett–Teller (BET) SSAs computed for ANS and ANLS-2 are 7 and 23 m^2 g^{-1}, respectively. Meanwhile, the BJH plot (Fig. 5a) reveals the pore size distribution of both the hydrochars, which shows a well-developed meso-microporous structure. Further, the minor hysteresis area formed in the moderate pressure range (P/P_o) of 0.55 to 0.99 of the N$_2$ adsorption/desorption isotherm also verifies the existence of mesopores along with a minor amount of macropores.[47] Additionally, the average pore diameter and the total pore volume for ANS hydrochar are estimated to be 43.95 nm and 0.05 cm^3 g^{-1}, respectively, and 18.28 nm and 0.19 cm^3 g^{-1} for ANLS-2, respectively. Consequently, the proliferated functional groups over the porous structure surface and superior SSA of ANLS-2 can facilitate CO$_2$ adsorption and bio-reduction over the cathode, enhancing acetate production compared to ANS.

The superimposed Raman spectra shed light on the molecular environment of the synthesized ANS and ANLS-2 hydrochars (Fig. 5b). It can be used to monitor the strength of D and G bands representing sp^3 (defective) and sp^2 (graphitic) carbon, appearing at 1376 cm^{-1} and 1578 cm^{-1}, respectively.[48] An increase in the intensity ratio of the D band to G band (I_D/I_G) elucidates the extent of disorder in the carbon lattice of the synthesized hydrochar.[49] The I_D/I_G ratio observed for ANS is 0.74, and for ANLS-2 is 0.68. The augmentation in graphitization of the carbon lattice of ANLS-2, along with higher SSA, accelerates electron mobility, which may be a plausible reason for the low R_{ct} (34.0 Ω) observed during the EIS analysis.

The elemental composition on the surface of ANLS-2 and ANS was examined *via* X-ray photoelectron spectroscopy (XPS). Both samples exhibited C, N, O, Al, and Si elements (Table S1†) at their respective binding energies (Fig. S4†). Further analysis of the C 1s core level spectrum (Fig. 5c) revealed various functional groups present in ANLS-2, including C=C/C–(C, H) at

284.5 eV, C–(O, N) at 285.3 eV, and C=O/O–C–O bonds at 288.4 eV, with a satellite peak observed at 292.3 eV, indicating a π–π bond (Fig. 4a).[50,51] Similar functional groups were detected in ANS, albeit without the satellite peak. Notably, the percentage of C=O/O–C–O in ANS (10.17%) was lower than that in ANLS-2 (44.58%) (Fig. 4b). Analysis of the O 1s spectrum revealed consistent bands in both hydrochars at 530.3 eV (–O–C), 532.6 eV (–C=O), and 534.1 eV (C–OH/C–O–C) (Fig. 5e). The deconvolution of the Al 2p (Fig. 5f) region resulted in peaks corresponding to Al(OH)$_3$ and Al–N bonds at 76.1 eV and 72.6 eV, respectively. The N 1s spectrum analysis showed peaks attributed to pyridinic, pyrrolic, and graphitic N, with an increase in pyridinic and graphitic N fractions observed in ANLS-2 (24.01% and 32.62%) compared to ANS (6.64% and 12.62%). These findings suggest that HTC enhances the formation of stable nitrogen-containing groups, which can act as active sites in CO$_2$ reduction, thereby improving the electrochemical activity and performance of MES. The pyridinic N contributes to the H$_2$ evolution reaction activity by reducing the overpotential, while graphitic N enhances current density by improving the electrical conductivity.

3.3. Product synthesis in MES

The performance of the as-synthesized ANLS-2 hydrochar in MES-ANLS for CO$_2$ sequestration and synthesizing multi-carbon organic compounds (Fig. S5a†) was elucidated by comparing it with MES operated with bare carbon felt at the cathode (MES-C) under similar operating conditions. Initially, both reactors were sparged with CO$_2$ for 10 days without imposing any potential, following which the cathodic potential was increased step-wise at a rate of −0.1 V *vs.* SHE per day until it reached −0.8 V *vs.* SHE. The slow transition in cathodic potential helped in the acclimation of homoacetogens on the negatively charged cathode. The mentioned cathodic potential was attained by increasing the cell voltage using the DC power supply.

Initially, the MES–ANLS had a slower startup (4.33 mM L^{-1}) compared to MES-C (7.58 mM L^{-1}), leading to lower acetate production until day 9 (Fig. 7a). This could be due to the negative surface charge of the hydrochar coated on the cathode.[52,53] In the cathodic chamber of MES, electrostatic repulsive forces between the negatively charged microorganisms and the cathode makes the formation of biofilm on the cathode challenging initially.[54] However, the acetate production rate in MES-ANLS gradually increased from day 12, reaching 3.79 ± 0.87 mM L^{-1} day^{-1} by day 27, which is about 2.52 times higher than the peak rate in MES-C observed on day 24 (Fig. 7b). The maximum acetate accumulation over a 33 days batch period in MES-ANLS was 41.14 ± 5.03 mM L^{-1}, approximately twice that of MES-C (Fig. 7a).

In addition to acetate, other carboxylic acids, such as iso-butyrate (Fig. S6c†) and propanoate (Fig. S6a†), were also detected. Initially, iso-butyrate concentrations were 1.03 mM L^{-1} in MES-C and 0.83 mM L^{-1} in MES-ANLS at the start of the batch cycle. These concentrations later increased to 3.79 ± 0.04 mM L^{-1} in MES-ANLS and 2.94 ± 0.11 mM L^{-1} in MES-C on day 33. On the other hand, despite the rise in propanoate
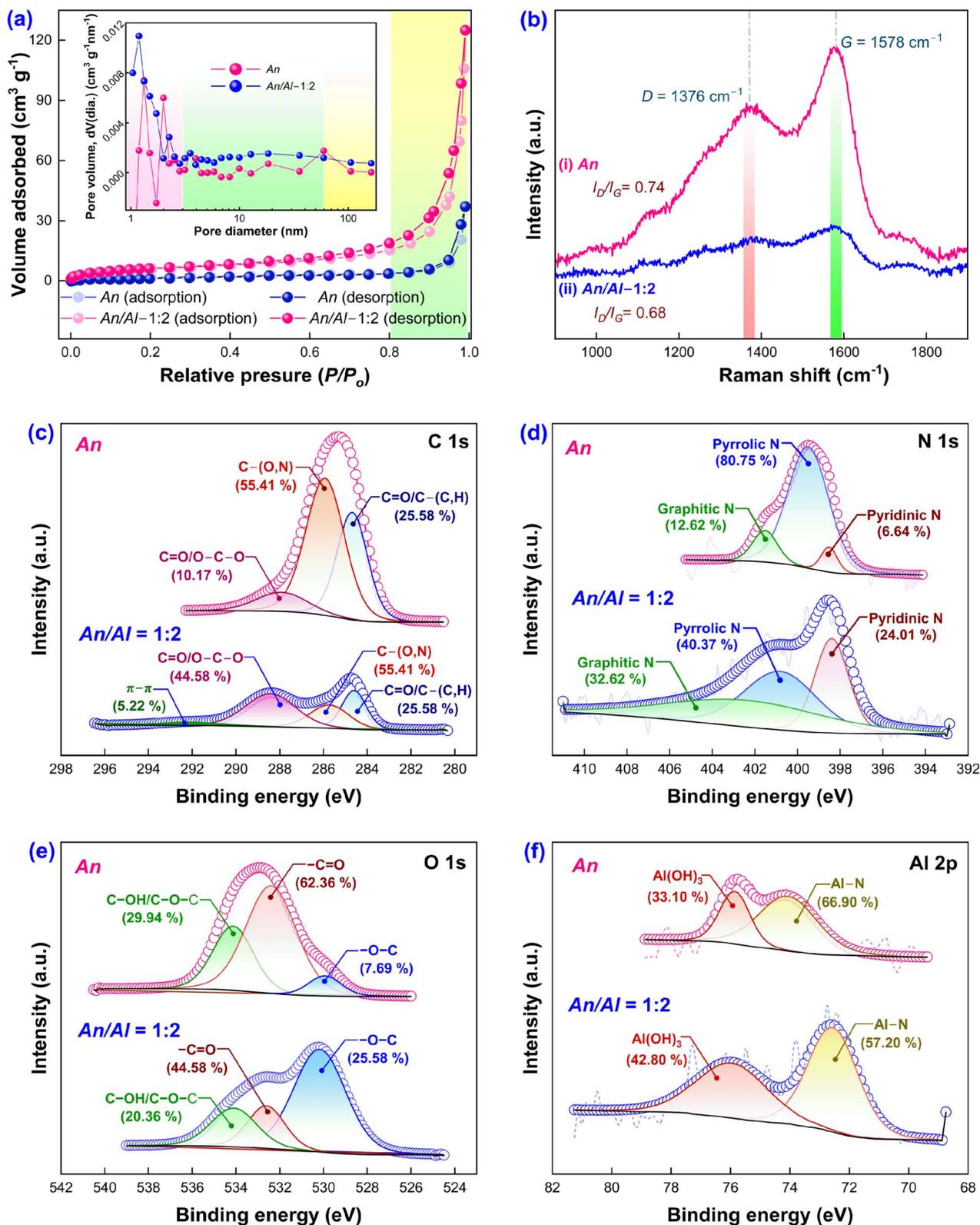
Fig. 5 (a) N$_2$ adsorption–desorption isotherms of ANS and ANLS-2 at −196 °C. The inscribed plot presents the pore size distribution curves of ANS and ANLS-2. (b) Raman spectra of (i) ANLS-2 and (ii) ANS hydrochars. Deconvoluted high-resolution (c) C 1s, (d) N 1s, (e) O 1s, and (f) Al 2p XPS spectra of the synthesized electrocatalysts ANS and ANLS-2 hydrochar.
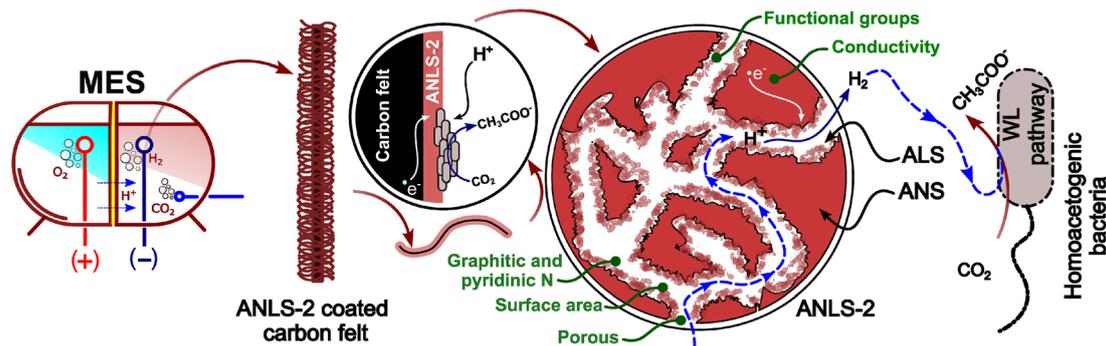
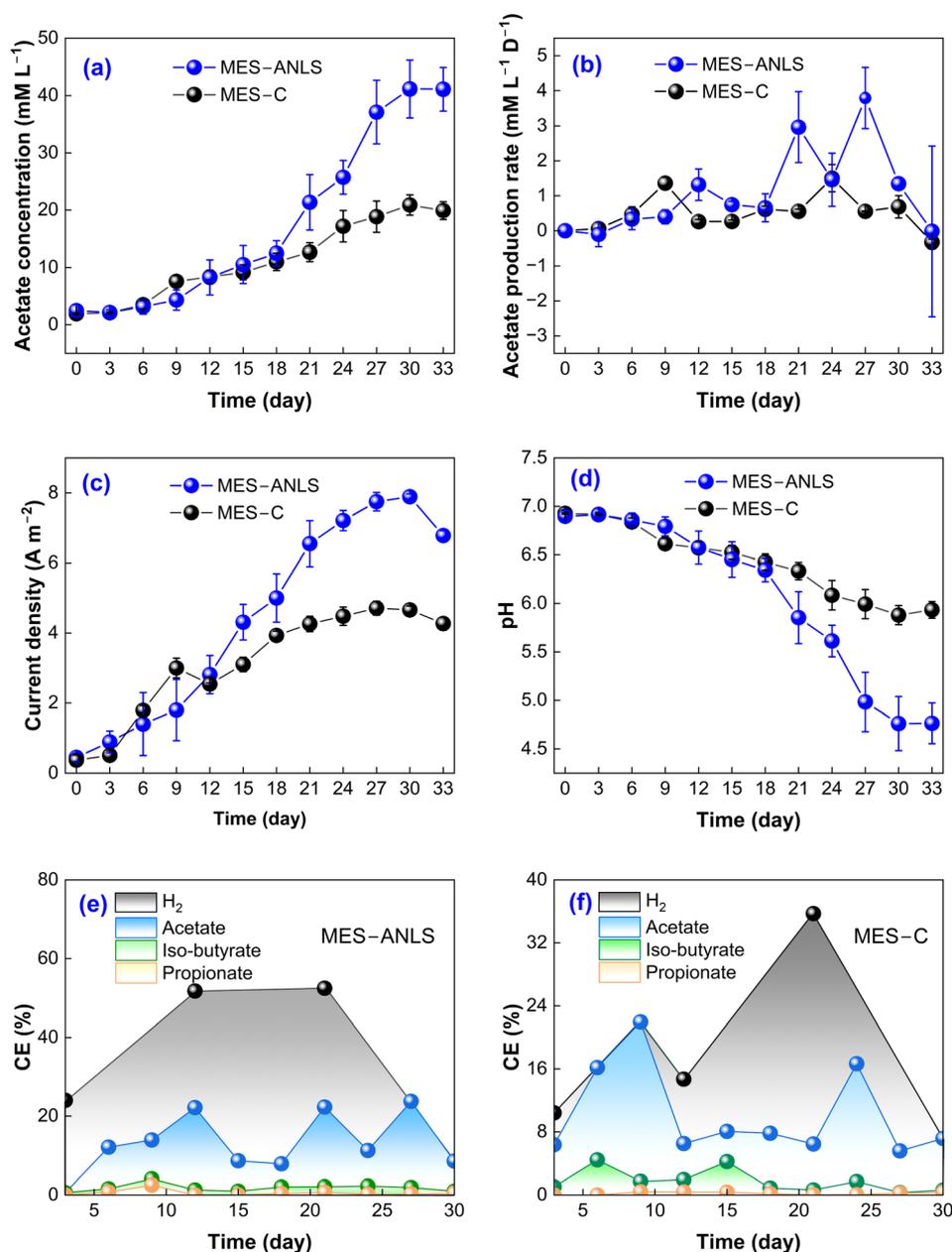Fig. 6   Schematic of CO_2 bioreduction to acetate at the ANLS-2 coated MES cathode through direct and indirect electron pathways.

Fig. 7   (a) Acetate concentration accumulated over the batch period of 33 days and (b) acetate production rates of MES-ANLS and MES-C. (c) pH variation recorded during the batch period (d) and current density recordings. (e) Cumulative current efficiency determined for MES-ANLS and (f) MES-C.

production, its accumulation by the end of the batch cycle remained low, reaching 1.06 ± 0.22 mM L^{-1} in MES-ANLS and 0.56 ± 0.12 mM L^{-1} in MES-C. These observations indicate that acetate was the dominant organic acid synthesized in the present investigation.

Apart from organics, H_2 was found to be accumulating in the headspace of both MES-ANLS and MES-C (Fig. S5a†). The headspace gas analysis revealed the predominance of H_2 compared to CO_2. This was because the gas bag attached to the MES was disconnected during CO_2 sparging. CH_4 was never detected during the entire investigation, indicating that the heat and chemical inhibition pretreatment eliminated methanogens in the inoculum. In MES-ANLS, the H_2 production rate gradually increased from 0.45 ± 0.13 mM L^{-1} day^{-1} on day 3 to a maximum of 4.46 ± 1.27 mM L^{-1} day^{-1} on day 33, which was 1.53 times that of MES-C. Although biofilm formation was visually evident in both MES reactors, the production of organic acids was predominantly dependent on H_2 (Fig. 6). Additionally, the higher H_2 production rate in MES-ANLS can be attributed to the presence of pyridinic N (Fig. 5d) in the ANLS-2, which promotes the H_2 evolution reaction, reducing the overpotential losses.

Initially, the pH of the catholyte was close to neutral (*i.e.*, 6.8). However, during the batch operation, it dropped to as low as 5 by day 27 in MES-ANLS. This decline in pH paralleled the trend of acetate synthesis, with increasing acetate concentration leading to lower pH. When the pH fell below 5, it caused product inhibition, which created unfavorable conditions for the homoacetogenic bacteria and hindered acetate production. Consequently, acetate synthesis was minimal after day 27. In MES-C, although the pH did not drop below 5, a similar trend was observed, possibly due to localized pH reduction in the microenvironment near the electrode, resulting in a decrease in product synthesis.[55] However, the buffering effect of hydrochar in MES-ANLS helped to maintain more stable conditions favouring the metabolism of homoacetogens, resulting in higher acetate production compared to MES-C.[22,23]

3.4. Cathodic current density

The quantity of electrons reaching the cathode elucidates the product generation rate in the cathodic chamber.[56] It was observed that from the initial startup, there was a gradual increase in the current density in both MES-ANLS and MES-C, starting from 0.37 A m^{-2}. It stabilized around day 24, attaining a maximum of 7.89 ± 0.80 and 4.71 ± 0.20 A m^{-2}, respectively (Fig. 7c). Thus, it was evident that the homoacetogens in the cathodic chamber of MES-ANLS were more effective in accepting the incoming electrons and reducing CO_2 into organics along with H_2 production compared to MES-C. The accumulation of acetate around the cathode in the cathodic chamber, combined with low pH in the microenvironment due to lack of mixing, may have led to product inhibition. This could explain the decreased acetate concentration and reduced current density after day 30. Additionally, the planktonic microbes benefited from the reduced overpotential for carrying out the H_2 evolution reaction by ANLS-2, as inferred in LSV analysis, supporting the H_2-mediated electron transfer. This was also verified by the enhanced rates of H_2 production in MES-ANLS compared to MES-C.

3.5. Coulombic and carbon recovery efficiency

The efficiency of the MES system in translating the reducing equivalents like electrons in the form of current and transforming CO_2 into organic products is disclosed using CE.[57] The CE is evaluated based on the production rates of the organic products and byproducts synthesized, as well as the current density recorded. Therefore, a higher production rate at a specific current density would produce a superior CE.[58] Low iso-butyric and propionic acid production rates contributed to a cumulative CE of less than 5% (Fig. 7e and f). In contrast, the CE of acetic acid alone was as high as 21.85% in MES-ANLS and 20.23% in MES-C. However, the highest CE was obtained for H_2 production, with 30.14% and 31.62% in MES-ANLS and MES-C, respectively. The higher H_2 production in MES-C demonstrates that the operational conditions here intensified the discrepancy between the utilization of reducing equivalents for H_2 generation over CO_2 reduction.[59] The overall CE, considering isobutyric, propionic, and acetic acids along with H_2, was as high as 52.44% in MES-ANLS and 35.71% in MES-C. Hence, based on the CE, it can be inferred that ANLS-2 enhanced the product synthesis in MES when applied as a cathode catalyst (Fig. 6). Table 1 summarises the performance comparison of ANLS-2 with the previous investigations reported in the literature based on area-specific production rates and CE.

Table 1 Performance comparison of MES with that reported in the literature

Cathode material	Inoculum	Cathodic potential (V vs. SHE)	Acetate concentration (mM L^{-1} day^{-1})	Coulombic efficiency (%)	Reference
Pt@C	Raw active sludge	−0.81	4.78	86.4	60
CuO/g-C$_3$N$_4$/rGO	Mixed culture	−0.65	4.50	—	61
EC-100 graphite granules	Cow rumen	−0.99	3.40	41	62
RGO–SiO$_2$–TiO$_2$	Mixed culture	−0.76	3.21	78	63
Co$_3$O$_4$/C	Mixed culture	−0.80	3.16	—	64
N-doped carbon dots	River sediment	−0.70	2.1	91.3	65
Carbon cloth	Anaerobic-activated sludge	−0.80	1.95	73.5	66
Graphite block	*Clostridium ljungdahlii*	−0.67	1.83	87	67
Platinum spiral wires	*Moorella thermoacetica*	−0.56	0.65	88.7	68
ANLS-2	UASB sludge	−0.80	3.79 ± 0.87	52.44	Present investigation

The extent of CO_2 reduction by the homoacetogens in the cathodic chamber is measured by CRE. The carbon substrate supplied to the system was in the form of CO_2, which was constant at all times, *i.e.*, 5 mL min^{-1} for 20 min daily, ensuring saturation of the dissolved CO_2 in the catholyte. The continuous sparging of CO_2 can fill the attached gas bag, and hence, this bag was disconnected during substrate feeding. The CRE observed in MES-ANLS and MES-C was majorly contributed by acetate, iso-butyrate, and propionate (Fig. S4e and f†). The CRE obtained for acetate was 31.83% in MES-ANLS and 16.16% in MES-C. However, the CRE contributed by the organic acids combined was 45.44% in MES-ANLS and 18.6% in MES-C.

3.6. Economic perspective

An economic analysis was performed to evaluate the cost of producing 1 L of acetic acid *via* the present MES configuration, and it was compared to the cost of commercial-grade glacial acetic acid (Tables S2–S4†). The analysis included the synthesis cost of ANLS-2 hydrochar and the operational expenses of MES. The cost of producing 1 L of acetic acid through MES was found to be \$3.43 (excluding downstream separation), while the price of commercial glacial acetic acid is ~\$6 (SRL India). Thus, the MES system utilised enables production of acetic acid at nearly 1.75-fold lower cost, which is further likely to reduce when the technology is implemented on a field scale due to more optimised usage of electrical equipment.

Further, the H_2 produced at the cathode holds significant economic value and can be used for industrial and commercial applications. The cost of electrolytes (Table S3†) can be avoided by using secondary treated effluent as the catholyte, thereby minimizing the requirement of chemical salts. For MES to become a more viable and sustainable option, improvements must be made to increase product yields and optimize downstream separation processes, which would enhance overall cost-efficiency.

Moreover, MES, if integrated into a WWTP where CO_2 is produced during aerobic and anaerobic processes, can be directly fed in the cathodic chamber of MES. Additionally, the oxygen generated in the anodic chamber can support biological aerobic treatment or serve as a precursor for ozone production during tertiary treatment. On the other hand, carrying out biological wastewater treatment in the anodic chamber can further lower external electricity demand. This integration will support simultaneous wastewater treatment and reduction of the carbon footprint of the WWTP.

Hence, the catalyst ANLS-2 facilitated CO_2 reduction into economically valuable and environmentally friendly compounds in the cathodic chamber approximately 2.44 times higher than that of bare graphite felt. The superior performance of ANLS-2 can be attributed to its beneficial structural properties, including a higher SSA, the presence of graphitic N, lower charge transfer resistance, and increased charge transfer capacity. These characteristics contribute to improved coulombic efficiency and carbon recovery in MES-ANLS. In contrast, recent research has shown cathode catalysts like zinc and molybdenum-based metal–organic frameworks (5.16 mM L^{-1} day^{-1}) synthesized *via* HTC and materials such as nickel foam (266.67 mM L^{-1}) have exceptional acetate production rates.[7,69] However, the present investigation addresses the challenges of sludge disposal from water and WWTPs by offering a facile synthesis of electrocatalysts for MES, supporting its scalability to field applications.

The incorporation of waste-derived transition metals, such as scrap iron, cobalt, or copper, into the present hydrochar composite could further improve the conductivity, resulting in greater product titres. Furthermore, overcoming the present reactor limitations, such as ensuring proper catholyte mixing, designing reactors capable of handling higher H_2 partial pressures and employing a stable and robust anode such as a mixed metal oxide electrode, can enhance acetate synthesis. Additionally, optimizing the CO_2 gas sparging volume as well as the imposed cathodic potential can considerably enhance the present CE and CRE. Therefore, the present investigation not only addresses the bottlenecks of MES but also offers a sustainable solution that supports the concept of a circular economy.

4. Conclusion

The application of ANLS-2 as a cathode catalyst coated over graphite felt demonstrated exemplary performance in MES by providing an acetate production rate as high as 3.79 ± 0.87 mM L^{-1} day^{-1} (2.37 ± 0.54 M m^{-2} day^{-1}) when compared to bare graphite felt. The exceptional properties of ANLS-2 that enhanced the product synthesis were mainly high SSA, copious functional groups on the hydrochar surface, high electrical conductivity, low charge transfer resistance, and the presence of N majorly as pyridinic N and graphitic N. This was also evident when the reported CE was 52.44% and CRE was 45.44% in the case of ANLS-2, which was 1.47 and 2.44 times that of bare graphite felt, respectively. Therefore, these results demonstrate the potential of exploring a sludge-derived cathode catalyst that can potentially enhance CO_2 bio-electrosynthesis in MES.

Data availability

Data will be made available upon request.

Author contributions

Lakshmi Pathi Thulluru: investigation, conceptualization, methodology, data curation, writing – original draft. Anil Dhanda: investigation, data curation, writing – original draft. Manikanta Manmadha Doki: investigation, data curation. Makarand M. Ghangrekar: supervision, validation, resources, writing – review & editing, funding acquisition. Shamik Chowdhury: supervision, validation, resources, writing – review & editing, funding acquisition.

Conflicts of interest

There are no conflicts to declare.

Acknowledgements

References

1 A. Ghorai, S. Roy, S. Das, H. Komber, M. M. Ghangrekar, B. Voit and S. Banerjee, Chemically stable sulfonated polytriazoles containing trifluoromethyl and phosphine oxide moieties for proton exchange membranes, *ACS Appl. Polym. Mater.*, 2020, **2**(7), 2967–2979, DOI: **10.1021/acsapm.0c00443**.

2 B. E. Logan, R. Rossi, A. A. Ragab and P. E. Saikaly, Electroactive microorganisms in bioelectrochemical systems, *Nat. Rev. Microbiol.*, 2019, **17**(5), 307–319, DOI: **10.1038/s41579-019-0173-x**.

3 A. Prévoteau, J. M. Carvajal-Arroyo, R. Ganigué and K. Rabaey, Microbial electrosynthesis from CO_2: forever a promise?, *Curr. Opin. Biotechnol.*, 2020, **62**, 48–57, DOI: **10.1016/j.copbio.2019.08.014**.

4 Y. He, J. Li, L. Zhang, X. Zhu, Q. Fu, Y. Pang and Q. Liao, Nano zero-valent iron functioned 3D printing graphene aerogel electrode for efficient solar-driven biocatalytic methane production, *Renewable Energy*, 2024, **11**, 120146, DOI: **10.1016/j.renene.2024.120146**.

5 J. Yin, K. Zhang, Y. Zhou, X. L. Li, T. Song and J. Xie, Co_3O_4/C derived from ZIF-67 cathode enhances the microbial electrosynthesis of acetate from CO_2, *Int. J. Hydrogen Energy*, 2024, **58**, 426–432, DOI: **10.1016/j.ijhydene.2024.01.210**.

6 L. Jourdin, S. Freguia, V. Flexer and J. Keller, Bringing high-rate, CO_2-based microbial electrosynthesis closer to practical implementation through improved electrode design and operating conditions, *Environ. Sci. Technol.*, 2016, **50**(4), 1982–1989, DOI: **10.1021/acs.est.5b04431**.

7 Y. Bian, A. Leininger, H. D. May and Z. J. Ren, H_2 mediated mixed culture microbial electrosynthesis for high titer acetate production from CO_2, *Environ. Sci. Ecotechnology*, 2024, **19**, 100324, DOI: **10.1016/j.ese.2023.100324**.

8 S. Bajracharya, B. Bian, R. Jimenez-Sandoval, L. Matsakas, K. P. Katuri and P. E. Saikaly, Nature inspired catalysts: a review on electroactive microorganism-based catalysts for electrochemical applications, *Electrochim. Acta*, 2024, **488**, 144215, DOI: **10.1016/j.electacta.2024.144215**.

9 S. Grover and L. E. Doyle, Advanced electrode materials for microbial extracellular electron transfer, *Trends Chem.*, 2024, **6**(3), 144–158, DOI: **10.1016/j.trechm.2024.01.005**.

10 T. Zhang, H. Nie, T. S. Bain, H. Lu, M. Cui, O. L. Snoeyenbos-West, A. E. Franks, K. P. Nevin, T. P. Russell and D. R. Lovley, Improved cathode materials for microbial electrosynthesis, *Energy Environ. Sci.*, 2013, **6**(1), 217–224, DOI: **10.1039/C2EE23350A**.

11 L. Jourdin, S. Freguia, B. C. Donose, J. Chen, G. G. Wallace, J. Keller and V. Flexer, A novel carbon nanotube modified scaffold as an efficient biocathode material for improved microbial electrosynthesis, *J. Mater. Chem. A*, 2014, **2**(32), 13093–13102, DOI: **10.1039/C4TA03101F**.

12 L. Jourdin, T. Grieger, J. Monetti, V. Flexer, S. Freguia, Y. Lu, J. Chen, M. Romano, G. G. Wallace and J. Keller, High acetic acid production rate obtained by microbial electrosynthesis from carbon dioxide, *Environ. Sci. Technol.*, 2015, **49**(22), 13566–13574, DOI: **10.1021/acs.est.5b03821**.

13 L. Chen, P. L. Tremblay, S. Mohanty, K. Xu and T. Zhang, Electrosynthesis of acetate from CO_2 by a highly structured biofilm assembled with reduced graphene oxide–tetraethylene pentamine, *J. Mater. Chem. A*, 2016, **4**(21), 8395–8401, DOI: **10.1039/C6TA02036D**.

14 M. Cui, H. Nie, T. Zhang, D. Lovley and T. P. Russell, Three-dimensional hierarchical metal oxide–carbon electrode materials for highly efficient microbial electrosynthesis, *Sustain. Energy Fuels*, 2017, **1**(5), 1171–1176, DOI: **10.1039/C7SE00073A**.

15 M. F. Alqahtani, K. P. Katuri, S. Bajracharya, Y. Yu, Z. Lai and P. E. Saikaly, Porous hollow fiber nickel electrodes for effective supply and reduction of carbon dioxide to methane through microbial electrosynthesis, *Adv. Funct. Mater.*, 2018, **28**(43), 1804860, DOI: **10.1002/adfm.201804860**.

16 T. Song, H. Zhang, H. Liu, D. Zhang, H. Wang, Y. Yang, H. Yuan and J. Xie, High efficiency microbial electrosynthesis of acetate from carbon dioxide by a self-assembled electroactive biofilm, *Bioresour. Technol.*, 2017, **243**, 573–582, DOI: **10.1016/j.biortech.2017.06.164**.

17 Y. Bian, A. Leininger, H. D. May and Z. J. Ren, H_2 mediated mixed culture microbial electrosynthesis for high titer acetate production from CO_2, *Environ. Sci. Ecotechnology*, 2024, **19**, 100324, DOI: **10.1016/j.ese.2023.100324**.

18 S. Tian, J. He, H. Huang, T. S. Song, X. Wu, J. Xie and W. Zhou, Perovskite-based multifunctional cathode with simultaneous supplementation of substrates and electrons for enhanced microbial electrosynthesis of organics, *ACS Appl. Mater. Interfaces*, 2020, **12**(27), 30449–30456, DOI: **10.1021/acsami.0c07910**.

19 Á. Ramírez, M. Muñoz-Morales, E. López-Fernández, F. J. Fernández-Morales and J. Llanos, Advancing circular economy: Critical insights into waste biomass derived carbon electrodes for (bio)electrochemical water treatment, *Curr. Opin. Electrochem.*, 2024, **46**, 101492, DOI: **10.1016/j.coelec.2024.101492**.

20 I. Chakraborty, S. Sathe, B. Dubey and M. Ghangrekar, Waste-derived biochar: Applications and future perspective in microbial fuel cells, *Bioresour. Technol.*, 2020, **312**, 123587, DOI: **10.1016/j.biortech.2020.123587**.

21 M. Cavali, N. Libardi Junior, R. D. A. Mohedano, P. Belli Filho, R. H. R. Da Costa and A. B. De Castilhos Junior, Biochar and hydrochar in the context of anaerobic digestion for a circular approach: An overview, *Sci. Total*

Environ., 2022, **822**, 153614, DOI: **10.1016/j.scitotenv.2022.153614**.

22 Z. Zhang, Z. Zhu, B. Shen and L. Liu, Insights into biochar and hydrochar production and applications: A review, *Energy*, 2019, **171**, 581–598, DOI: **10.1016/j.energy.2019.01.035**.

23 Q. Xu, L. Luo, D. Li, D. Johnravindar, S. Varjani, J. W. Wong and J. Zhao, Hydrochar prepared from digestate improves anaerobic co-digestion of food waste and sewage sludge: Performance, mechanisms, and implication, *Bioresour. Technol.*, 2022, **362**, 127765, DOI: **10.1016/j.biortech.2022.127765**.

24 P. D. Dissanayake, S. You, A. D. Igalavithana, Y. Xia, A. Bhatnagar, S. Gupta, H. W. Kua, S. Kim, J. Kwon, D. C. Tsang and Y. S. Ok, Biochar-based adsorbents for carbon dioxide capture: A critical review, *Renew. Sustain. Energy Rev.*, 2020, **119**, 109582, DOI: **10.1016/j.rser.2019.109582**.

25 W. Zhao, H. Xie, J. Li, L. Zhang and Y. Zhao, Application of alum sludge in wastewater treatment processes: "Science" of reuse and reclamation pathways, *Processes*, 2021, **9**(4), 612, DOI: **10.3390/pr9040612**.

26 S. M. Yusuff, O. K. Khim, W. Md Zin Man Yunus, M. Ahmad, N. Ibrahim, F. C. Ros and T. CC, Carbon dioxide sorption isotherm and kinetics by alum sludge, *Mater. Today: Proc.*, 2018, **5**(10), 21948–21955, DOI: **10.1016/j.matpr.2018.07.055**.

27 K. Tahir, W. Miran, J. Jang, N. Maile, A. Shahzad, M. Moztahida, A. A. Ghani, B. Kim, H. Jeon and D. S. Lee, MXene-coated biochar as potential biocathode for improved microbial electrosynthesis system, *Sci. Total Environ.*, 2021, **773**, 145677, DOI: **10.1016/j.scitotenv.2021.145677**.

28 G. Soggia, A. Goglio, P. Cristiani, I. Luciani, E. Clagnan and F. Adani, Bioelectrochemical protein production valorising NH₃-rich pig manure-derived wastewater and CO₂ from anaerobic digestion, *Renewable Energy*, 2024, **229**, 120761, DOI: **10.1016/j.renene.2024.120761**.

29 C. Li, Y. Liu, M. Luo, J. Cao, F. Fang, Q. Feng, J. Luo, L. Hao and C. Wang, Enhancing simultaneous electrosynthesis of CO₂ and nitrogen removal in microbial fuel cell (MFC) cathode compartment by adding Fe–C/biochar compound substrates, *J. Power Sources*, 2023, **560**, 232707, DOI: **10.1016/j.jpowsour.2023.232707**.

30 S. Bajracharya, R. Yuliasni, K. Vanbroekhoven, C. J. Buisman, D. P. Strik and D. Pant, Long-term operation of microbial electrosynthesis cell reducing CO₂ to multi-carbon chemicals with a mixed culture avoiding methanogenesis, *Bioelectrochemistry*, 2017, **113**, 26–34, DOI: **10.1016/j.bioelechem.2016.09.001**.

31 S. Das, S. Das and M. M. Ghangrekar, Application of TiO₂ and Rh as cathode catalyst to boost the microbial electrosynthesis of organic compounds through CO₂ sequestration, *Process Biochem.*, 2021, **101**, 237–246, DOI: **10.1016/j.procbio.2020.11.017**.

32 Y. Li, S. Chen, X. Wu, H. Zhang and J. Zhang, A hybrid zeolitic imidazolate framework-derived ZnO/ZnMoO₄

33 heterostructure for electrochemical hydrogen production, *Dalton Trans.*, 2021, **50**(33), 11365–11369, DOI: **10.1039/D1DT01861B**.

33 Y. Yang, Y. Q. Zhao and P. Kearney, Influence of ageing on the structure and phosphate adsorption capacity of dewatered alum sludge, *Chem. Eng. J.*, 2008, **145**(2), 276–284, DOI: **10.1016/j.cej.2008.04.026**.

34 C. Zhang, Z. Xu, Y. Hu, J. He, M. Tian, J. Zhou, Q. Zhou, S. Chen, D. Chen, P. Chen and W. Sun, Novel insights into the hydroxylation behaviors of α-quartz (101) surface and its effects on the adsorption of sodium oleate, *Minerals*, 2019, **9**(7), 450, DOI: **10.3390/min9070450**.

35 L. Feng, Y. Zou, Y. Zhao, Z. Wang, J. Liu and X. Gong, Hydroxyl Removal in Muscovite by Heating for Low-Fluoride Purification of Natural Flake Graphite, *Energy Fuels*, 2024, **38**(3), 2436–2446, DOI: **10.1021/acs.energyfuels.3c04113**.

36 L. de Siqueira, C. G. de Paula, R. F. Gouveia, M. Motisuke and E. de Sousa Trichês, Evaluation of the sintering temperature on the mechanical behavior of β-tricalcium phosphate/calcium silicate scaffolds obtained by gelcasting method, *J. Mech. Behav. Biomed. Mater.*, 2019, **90**, 635–643, DOI: **10.1016/j.jmbbm.2018.11.014**.

37 C. Ni, C. Xia, W. Liu, W. Xu, Z. Shan, X. Lei and Z. Tao, Effect of Graphene on the Performance of Silicon–Carbon Composite Anode Materials for Lithium-Ion Batteries, *Materials*, 2024, **17**(3), 754, DOI: **10.3390/ma17030754**.

38 S. A. Khan, S. B. Khan, L. U. Khan, A. Farooq, K. Akhtar and A. M. Asiri, Fourier transform infrared spectroscopy: fundamentals and application in functional groups and nanomaterials characterization, *Handb. Mater. Charact.*, 2018, pp. 317–344, DOI: **10.1007/978-3-319-92955-2_9**.

39 C. F. Lin, S. H. Liu and O. J. Hao, Effect of functional groups of humic substances on UF performance, *Water Res.*, 2001, **35**(10), 2395–2402, DOI: **10.1016/S0043-1354(00)00525-X**.

40 W. Zheng, J. Du, Z. Wu, M. Yin, W. Liu and S. Han, Efficient and economical synthesis of flame retardant rigid polyurethane nanocomposite foam through phosphorus-based compounds and in-situ exfoliated microcrystal muscovite, *Polym.-Plast. Technol. Mater.*, 2024, **63**(4), 385–398, DOI: **10.1080/25740881.2023.2289063**.

41 J. D. O. Silva, M. G. R. Filho, S. D. Ribeiro, J. G. Vieira and C. V. Silva, Thermal analysis and FTIR studies of sewage sludge produced in treatment plants. The case of sludge in the city of Uberlândia-MG, Brazil, *Thermochim. Acta*, 2012, **528**, 72–75, DOI: **10.1016/j.tca.2011.11.010**.

42 Y. Y. He, X. C. Wang, P. K. Jin, B. Zhao and X. Fan, Complexation of anthracene with folic acid studied by FTIR and UV spectroscopies, *Spectrochim. Acta, Part A*, 2009, **72**(4), 876–879, DOI: **10.1016/j.saa.2008.12.021**.

43 P. Falaras, Synergetic effect of carboxylic acid functional groups and fractal surface characteristics for efficient dye sensitization of titanium oxide, *Sol. Energy Mater. Sol. Cells*, 1998, **53**(1–2), 163–175, DOI: **10.1016/S0927-0248(98)00023-3**.

44 Q. Wang, Q. Xu, Z. Du, W. Zhang, D. Wang and Y. Peng, Mechanistic insights into the effects of biopolymer

conversion on macroscopic physical properties of waste activated sludge during hydrothermal treatment: Importance of the Maillard reaction, *Sci. Total Environ.*, 2021, **769**, 144798, DOI: **10.1016/j.scitotenv.2020.144798**.

45 T. Wu, M. Y. Han and Z. J. Xu, Size effects of electrocatalysts: more than a variation of surface area, *ACS Nano*, 2022, **16**(6), 8531–8539, DOI: **10.1021/acsnano.2c04603**.

46 A. H. M. Videla, L. Osmieri, M. Armandi and S. Specchia, Varying the morphology of Fe-NC electrocatalysts by templating Iron Phthalocyanine precursor with different porous SiO_2 to promote the Oxygen Reduction Reaction, *Electrochim. Acta*, 2015, **177**, 43–50, DOI: **10.1016/j.electacta.2015.01.165**.

47 C. Schlumberger and M. Thommes, Characterization of hierarchically ordered porous materials by physisorption and mercury porosimetry—a tutorial review, *Adv. Mater. Interfaces*, 2021, **8**(4), 2002181, DOI: **10.1002/admi.202002181**.

48 A. V. Munde, B. B. Mulik, P. P. Chavan and B. R. Sathe, Enhanced electrocatalytic activity towards urea oxidation on Ni nanoparticle decorated graphene oxide nanocomposite, *Electrochim. Acta*, 2020, **349**, 136386, DOI: **10.1016/j.electacta.2020.136386**.

49 C. Zhang, B. Wang, X. Shen, J. Liu, X. Kong, S. S. Chuang and Z. Peng, A nitrogen-doped ordered mesoporous carbon/graphene framework as bifunctional electrocatalyst for oxygen reduction and evolution reactions, *Nano Energy*, 2016, **30**, 503–510, DOI: **10.1016/j.nanoen.2016.10.051**.

50 P. Hidalgo, R. Navia, R. Hunter, G. Coronado and M. Gonzalez, Synthesis of Carbon nanotubes using biochar as precursor material under microwave irradiation, *J. Environ. Manag.*, 2019, **244**, 83–91, DOI: **10.1016/j.jenvman.2019.03.082**.

51 J. Yeo, D. Seong and S. Hwang, Chemical surface modification of lignin particle and its application as filler in the polypropylene composites, *J. Ind. Eng. Chem.*, 2015, **31**, 80–85, DOI: **10.1016/j.jiec.2015.06.010**.

52 A. A. Azzaz, B. Khiari, S. Jellali, C. M. Ghimbeu and M. Jeguirim, Hydrochars production, characterization and application for wastewater treatment: A review, *Renew. Sustain. Energy Rev.*, 2020, **127**, 109882, DOI: **10.1016/j.rser.2020.109882**.

53 H. Li, Y. Zhang, J. Guo, J. Lv, W. Huan and B. Li, Preparation of hydrochar with high adsorption performance for methylene blue by co-hydrothermal carbonization of polyvinyl chloride and bamboo, *Bioresour. Technol.*, 2021, **337**, 125442, DOI: **10.1016/j.biortech.2021.125442**.

54 J. Zhang, H. Liu, Y. Zhang, P. Wu, J. Li, P. Ding, Q. Jiang and M. Cui, Heterotrophic precultivation is a better strategy than polarity reversal for the startup of acetate microbial electrosynthesis reactor, *Biochem. Eng. J.*, 2022, **179**, 108319, DOI: **10.1016/j.bej.2021.108319**.

55 J. A. Modestra, B. Navaneeth and S. V. Mohan, Bio-electrocatalytic reduction of CO_2: Enrichment of homoacetogens and pH optimization towards enhancement of carboxylic acids biosynthesis, *J. CO_2 Util.*, 2015, **10**, 78–87, DOI: **10.1016/j.jcou.2015.04.001**.

56 F. Harnisch, J. S. Deutzmann, S. T. Boto and M. A. Rosenbaum, Microbial electrosynthesis: Opportunities for microbial pure cultures, *Trends Biotechnol.*, 2024, **42**(8), 1035–1047, DOI: **10.1016/j.tibtech.2024.02.004**.

57 P. Dessì, L. Rovira-Alsina, C. Sánchez, G. K. Dinesh, W. Tong, P. Chatterjee, M. Tedesco, P. Farràs, H. M. Hamelers and S. Puig, Microbial electrosynthesis: Towards sustainable biorefineries for production of green chemicals from CO_2 emissions, *Biotechnol. Adv.*, 2020, **46**, 107675, DOI: **10.1016/j.biotechadv.2020.107675**.

58 H. M. Fruehauf, F. Enzmann, F. Harnisch, R. Ulber and D. Holtmann, Microbial Electrosynthesis—An Inventory on Technology Readiness Level and Performance of Different Process Variants, *Biotechnol. J.*, 2020, **15**(10), 2000066, DOI: **10.1002/biot.202000066**.

59 Y. Bian, A. Leininger, H. D. May and Z. J. Ren, H_2 mediated mixed culture microbial electrosynthesis for high titer acetate production from CO_2, *Environ. Sci. Ecotechnology*, 2024, **19**, 100324, DOI: **10.1016/j.ese.2023.100324**.

60 Y. Wang, S. Yu, X. Zheng, X. Wu, G. Pu, G. Wu, N. Chu, X. He, D. Li, R. Jianxiong Zeng and Y. Jiang, Delineating cathodic extracellular electron transfer pathways in microbial electrosynthesis: Modulation of polarized potential and Pt@C addition, *Bioresour. Technol.*, 2024, **402**, 130754, DOI: **10.1016/j.biortech.2024.130754**.

61 T. Li, K. Zhang, D. Luo, T. Song and J. Xie, CuO/g-C_3N_4/rGO multifunctional photocathode with simultaneous enhancement of electron transfer and substrate mass transfer facilitates microbial electrosynthesis of acetate, *Int. J. Hydrogen Energy*, 2022, **47**(82), 34875–34886, DOI: **10.1016/j.ijhydene.2022.08.066**.

62 I. Vassilev, J. M. Rinta-Kanto and M. Kokko, Comparing the performance of fluidized and fixed granular activated carbon beds as cathodes for microbial electrosynthesis of carboxylates from CO_2, *Bioresour. Technol.*, 2024, **403**, 130896, DOI: **10.1016/j.biortech.2024.130896**.

63 A. H. Anwer, M. Shoeb, F. Mashkoor, A. Ali, S. Kareem, M. Z. Ansari, J. M. Park and C. Jeong, Simultaneous reduction of carbon dioxide and energy harvesting using RGO-based SiO_2-TiO_2 nanocomposite for supercapacitor and microbial electrosynthesis, *Appl. Catal., B*, 2023, **339**, 123091, DOI: **10.1016/j.apcatb.2023.123091**.

64 J. Yin, K. Zhang, Y. Zhou, X. L. Li, T. Song and J. Xie, Co_3O_4/C derived from ZIF-67 cathode enhances the microbial electrosynthesis of acetate from CO_2, *Int. J. Hydrogen Energy*, 2024, **58**, 426–432, DOI: **10.1016/j.ijhydene.2024.01.210**.

65 J. Hu, C. Zeng, G. Liu, Z. J. Ren, H. Luo and M. Teng, Carbon dots internalization enhances electroactive biofilm formation and microbial acetate synthesis, *J. Clean. Prod.*, 2023, **411**, 137333, DOI: **10.1016/j.jclepro.2023.137333**.

66 H. Liu, Y. Zeng, W. Chen, C. Liu, D. Sun, Z. Hu, P. Li, H. Xu, H. Wu, B. Qiu, X. Liu and Y. Dang, Effect of different hydrogen evolution rates at cathode on bioelectrochemical reduction of CO_2 to acetate, *Sci. Total*

Environ., 2024, **913**, 169744, DOI: **10.1016/j.scitotenv.2023.169744**.

67 S. T. Boto, B. Bardl, F. Harnisch and M. A. Rosenbaum, Microbial electrosynthesis with *Clostridium ljungdahlii* benefits from hydrogen electron mediation and permits a greater variety of products, *Green Chem.*, 2023, **25**(11), 4375–4386, DOI: **10.1039/D3GC00471F**.

68 B. N. Ha, D. M. Pham, D. Masuda, T. Kasai and A. Katayama, Humin-promoted microbial electrosynthesis of acetate from CO_2 by *Moorella thermoacetica*, *Biotechnol. Bioeng.*, 2022, **119**(12), 3487–3496, DOI: **10.1002/bit.28238**.

69 Y. Chen, Y. Chen, D. Z. Dai, X. L. Li, T. Song and J. Xie, ZnMo-MOF as anti-CO hydrogen electrocatalyst enhance microbial electrosynthesis for CO/CO_2 conversion, *Chemosphere*, 2024, **358**, 142157, DOI: **10.1016/j.chemosphere.2024.142157**.